



جامعة الملك عبد الله
للعلوم والتقنية

King Abdullah University of
Science and Technology

Tuning of the conformation of asymmetric nonfullerene acceptors for efficient organic solar cells

Item Type	Article
Authors	Yang, Linqiang; Song, Xin; Yu, Jiangsheng; Wang, Hongtao; Zhang, Zhuohan; Geng, Renyong; Cao, Jinru; Baran, Derya; Tang, Weihua
Citation	Yang, L., Song, X., Yu, J., Wang, H., Zhang, Z., Geng, R., ... Tang, W. (2019). Tuning of the conformation of asymmetric nonfullerene acceptors for efficient organic solar cells. <i>Journal of Materials Chemistry A</i> , 7(39), 22279–22286. doi:10.1039/c9ta07634d
Eprint version	Post-print
DOI	10.1039/c9ta07634d
Publisher	Royal Society of Chemistry (RSC)
Journal	<i>Journal of Materials Chemistry A</i>
Rights	Archived with thanks to <i>Journal of Materials Chemistry A</i>
Download date	09/08/2022 16:02:42
Link to Item	http://hdl.handle.net/10754/660051

Asymmetric nonfullerene acceptors tuning conformation for efficient organic solar cells†

Linqiang Yang,^{a,‡} Xin Song,^{b,‡} Jiangsheng Yu,^c Hongtao Wang,^a Zhuohan Zhang,^a Renyong Geng,^a Jinru Cao,^a Derya Baran,^{*b} Weihua Tang,^{*a}

Received 00th January 20xx,
Accepted 00th January 20xx

DOI: 10.1039/x0xx00000x

www.rsc.org/

In this work, three dithieno[3,2-*b*:2',3'-*d*]pyrrol fused-ring electron acceptors (IPT-2F, IPTT-2F, and IPTTT-2F) have been successfully developed as efficient asymmetric nonfullerene acceptors (NFAs) for organic solar cells (OSCs). The molecular conformation of these NFAs can be subtly tuned by extending the donating cores with thiophene rings. Experimental and theoretical study indicate the crucial role of the conformation change in asymmetric NFAs played for the aggregation of their blend films with PBDB-T. Indeed, the blend films with S-shape IPT-2F and IPTTT-2F reveal less trap-assisted recombination and better microphase separation compared with the C-shape IPTT-2F. Decent power conversion efficiency (PCE) values of 14% and 12.3% were achieved for IPT-2F- and IPTTT-2F-based OSCs, respectively. Our results indicate the S-shape conformation of asymmetric NFAs locked via S...O interactions is advantageous to finetune the morphology in active layer for more efficient OSCs.

1. Introduction

Organic solar cells (OSCs) have shown ever-increasing potential for solar energy harvesting because of their evident advantages of lightweight, flexibility, transparency and low-cost fabrication.¹⁻⁴ With the great development in polymer donors, nonfullerene acceptors (NFAs) and device technology, OSCs have achieved a power conversion efficiency (PCE) over 15% and 16% in single-junction binary and ternary devices, respectively.⁵⁻⁹ Especially, fused-ring electron acceptors (FREAs) adopting acceptor-donor-acceptor (A-D-A) structure have triggered the rapid progress and beat fullerene-based acceptors, owing to their enhanced intramolecular charge transfer (ICT) to promote light absorption and electron mobility, suitable intermolecular stacking and aggregation to optimize morphology of blends with donors, as well better solution processability.¹⁰⁻¹¹ For molecular engineering of NFAs, most strategies focus on the fused donating core by adding or removing same aromatic rings on both sides to form symmetric structure. The classic ITIC or INIC series FREAs have been designed with conjugation extending on both sides of indacenodithiophene (IDT) core by fusing thiophene (T) or

thieno[3,2-*b*]thiophene (TT) units.¹²⁻¹⁶ To maintain the symmetry, two same electron-donating units are exploited to flank the core on both sides.¹⁷⁻¹⁹ For more precise regulation of FREAs' properties, asymmetric NFAs have been proposed as a subtle modification by changing only one side of D core. Importantly, the asymmetry is found to induce larger dipole moment in NFAs, leading to enhanced ICT and stronger intermolecular binding energy.²⁰ Under the actuation and induction of dipole moment, asymmetric NFAs can thus reinforce the molecular interactions to form a compact and well-organized intermolecular stacking.²¹ As such, asymmetric FREAs have been designed and synthesized by flanking one side of D cores with an electron-donating unit such as T, TT, and dithieno[3,2-*b*:2',3'-*d*]thiophene (TTT).²²⁻²⁷ The as-designed asymmetric NFAs have rendered high PCEs (10~13%) and fill factor (FF) (70~79%) in OSCs.²²⁻²⁷

Recently, our group have successfully explored dithieno[3,2-*b*:2',3'-*d*]pyrrol (DTP) as a good donating block^{28,29} to construct indacenobis(dithieno[3,2-*b*:2',3'-*d*]pyrrol) (INP) based FREAs.³⁰⁻³² The conjugation of occupied *p* orbitals of N and S heteroatoms with *p* orbitals of aromatic rings offers DTP with strong electron-donating capability, while electron-rich N atoms help to narrow down the bandgap and act as ideal site for sidechain engineering.^{30,32} The INP-cored symmetric FREA (INPIC-4F) featuring a 1.39 eV bandgap delivered 13.13% PCE and 71.5% FF when blending with PBDB-T as polymer donor.³⁰⁻³² The single-junction devices were further optimized by an asymmetric NFA (MeIC1) as the third component in ternary OSCs. An impressive PCE of 13.73% was achieved by matching absorption and photovoltaic parameters for corresponding two binary OSCs.³³ However, the crystallization of INPIC-4F needed to be retarded by

^a School of Chemical Engineering, Nanjing University of Science and Technology, Nanjing 210094, P.R. China. E-mail: whtang@njut.edu.cn.

^b KAUST Solar Center (KSC), King Abdullah University of Science and Technology (KAUST), Thuwal 23955-6900, Saudi Arabia. E-mail: derya.baran@kaust.edu.sa.

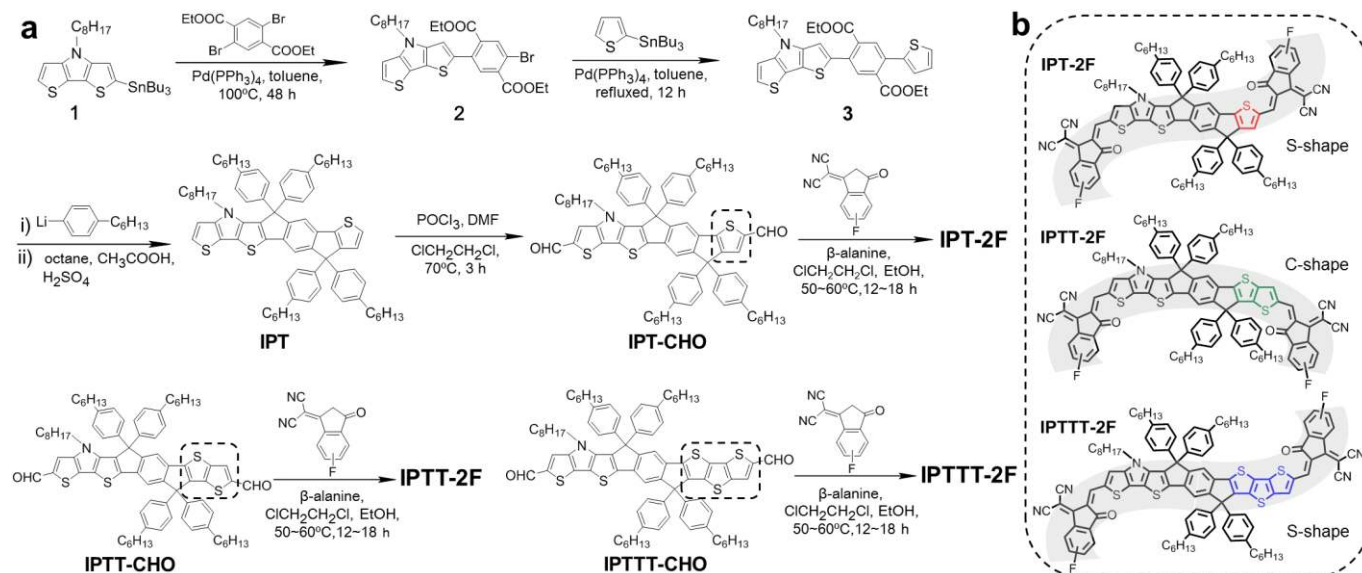
^c MIIT Key Laboratory of Advanced Solid Laser, Nanjing University of Science and Technology, Nanjing 210094, P.R. China.

† Electronic Supplementary Information (ESI) available: Materials synthesis and characterization, device fabrication, SCLC mobility, GIWAXS and summary of high-efficiency asymmetric NFAs OSCs in literature. See DOI: 10.1039/x0xx00000x.

‡ L. Y. and X. S. contributed equally to this work.

casting the blend films from hot substrates or binary solvents to encourage suitable π - π stacking,^{34,35} which is challenging for large-scale solution processing of OSCs. To address this, we have thus design asymmetric FREAs by replacing the DTP at one side of INP core with a smaller and weaker electron-donating unit including T, TT, and TTT, which are designated as **IPT-2F**, **IPTT-2F**, and **IPTTT-2F**,

respectively (Scheme 1). To match the weakened donating core, only single fluorinated 3-(dicyanomethylidene)indan-1-one (IC) accepting terminal was adopted for the asymmetric FREAs. The consequence of breaking asymmetry in the fused donating core intrigues us to explore the optoelectronic and photovoltaic properties of the resultant FREAs.



Scheme 1 (a) Synthetic routes to **IPT-2F**, **IPTT-2F**, and **IPTTT-2F**. (b) Molecular structures and preferred conformations of the three acceptors.

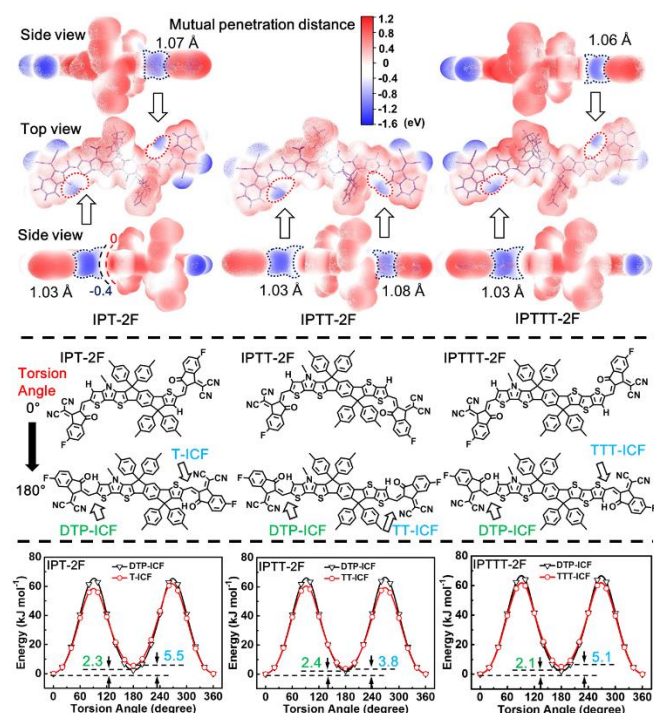


Fig. 1 Molecular surface electrostatic potential and van der Waals mutual penetration distance between oxygen atom and sulfur atom (top panel). Possible rotamers (middle panel) and potential energy surface scan (bottom panel) of three acceptors.

2. Results and Discussion

The synthetic route to our designed asymmetric FREAs is shown in Scheme 1a. The asymmetric D cores (IPT, IPTT, and IPTTT)

by flanking indeno[dithieno[3,2-b:2',3'-d]pyrrol] with T, TT or TTT units were constructed with a two-step approach involving Stille coupling and Friedel-Crafts intramolecular cyclization. The followed Vilsmeier reaction afforded the corresponding di-aldehydes in ~88% yields. The target **IPT-2F**, **IPTT-2F**, and **IPTTT-2F** were finally synthesized via Knoevenagel condensation between di-aldehydes and 2-(5/6-difluoro-3-oxo-2,3-dihydro-1*H*-inden-1-ylidene)malononitrile (IC-F). The optimized condensation must be conducted under the catalysis of β -alanine at $50\sim60^\circ\text{C}$ to realize higher yields ($>80\%$). The synthetic details and characterization data are presented in the Electronic Supplementary Information (Scheme S1, Fig. S1-S30, ESI†). Three NFAs have good solubility in common solvents and thermal stability with a decomposition temperature (T_d) over 330°C (corresponding to 5% weight loss in thermogravimetric analysis, Fig. S31a, ESI†).

Three asymmetric FREAs exhibit different molecular conformations due to the flanking of different thiophene fused rings in central core (Scheme 1b). It's known that the S atoms from thiophene ends in IPT (or IPTT, IPTTT) cores can construct noncovalent interactions with O atoms from IC-F.³⁶⁻³⁸ This weak intramolecular S...O "conformational locks" affords planar structure to promote π - π stacking and molecular packing in solid state. A C-shape conformation is observed for **IPTT-2F**, where two IC-F end groups aren't parallel aligned on the same side of IPTT core axis. Importantly, **IPT-2F** and **IPTTT-2F** adopt a S-shape conformation due to the parallel alignment of IC-F terminals. To further understand and confirm the preferred S-shape or C-shape conformation, we simulated the molecular surface electrostatic potential of the three acceptors with Multiwfn^{39,40} and VMD. As

shown in Fig. 1, negative electrostatic potentials of O atoms diffuse and penetrate to the surface of S atoms. Moreover, van der Waals mutual penetration distance (d) (O...S) was calculated by the difference between sum of non-bonded atomic radius and actual distance of O...S. The d values (O...S) of the three acceptors are all over 1 Å together with the electrostatic potential diffusion, which mean the existence of considerable weak interaction.^{41,42} Relaxed potential surface energy scans were further studied to understand the conformation energy of **IPT-2F**, **IPTT-2F** and **IPTTT-2F**. There are four potential rotamers in the acceptors, called as DTP-ICF, T-ICF, TT-ICF and TTT-ICF, respectively (Fig. 1). The energy values of the rotamers in the acceptors at torsion angle of 180° are all grater than those at 0° because of the steric hindrance effect of H atom. These results confirm the stable and preferred S-shape for **IPT-2F** and **IPTTT-2F** as well as C-shape for **IPTT-2F**.

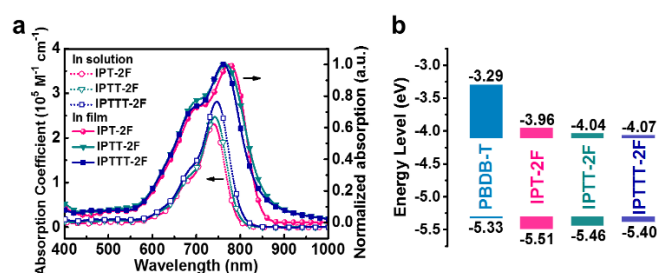


Fig. 2 (a) Absorption spectra of the acceptors in solution and neat films. (b) Energy level diagram of PBDB-T and the acceptors.

Table 1 Optical, electrochemical properties of the three acceptors.

Acceptor	λ_{\max}^a [nm]	λ_{\max}^b [nm]	λ_{\max}^c [nm]	$E_g^{\text{opt } c}$ [eV]	HOMO [eV]	LUMO [eV]
IPT-2F	739	775	857	1.44	-5.51	-3.96
IPTT-2F	742	766	874	1.42	-5.46	-4.04
IPTTT-2F	746	761	866	1.43	-5.40	-4.07

^a In chloroform solution with a concentration of 0.25×10^{-5} mol L⁻¹. ^b In thin film. ^c $E_g^{\text{opt}} = 1240/\lambda_{\text{onset}}$.

The optical spectra of three NFAs are plotted in Fig. 2a, with characteristic data listed in Table 1. In chloroform solution, slightly redshifted absorptions along with enhanced molar extinction coefficient are observed with the extension of π -conjugation to contribute intensified electron-donating ability from IPT to IPTT and IPTTT. Comparably, **IPT-2F** bearing the weakest donating core exhibits a largest red-shift (ca. 36 nm) in maximum absorption peak from solution to film. This result is an evidence for a more well-aligned and compact intermolecular stacking of **IPT-2F** molecules in solid state. It is believed that extending π -conjugation with electron-donating units in a weaker fused D core commonly can narrow optical bandgap (E_g^{opt}), and expectantly enlarges the J_{SC} . Song et al.²² successfully exploited asymmetric NFAs of TPT-2F, TPTT-2F, and TPTTT-2F with obviously enhanced D core in sequence. Red-shifted film absorption effectively increased the J_{SC} , providing the space for PCE improvement. In this regard, the conformation reversals of the acceptors leading to transformations of molecular packing and aggregation shouldn't become a restricted factor for PCE enhancement. We

hypothesized that DTP unit is such a strong electron-donating block that our asymmetric NFAs show unchanged optical absorption in film state, even blue-shifted with the extension of π -conjugation from **IPT-2F** to **IPTT-2F**, and **IPTTT-2F**. Similar results have been found for FREAs by extending the D core on the opposite side of TTT, which is used as the strong and dominant donor block. The resultant NFAs exhibit almost unchanged optical absorption when the flanking donating unit is changed from T to TT and TTT on the other side (Table S1 and the references inside, ESI†). For asymmetric FREAs bearing same number of fused rings in central core, our DTP-extended NFAs exhibit ~50 nm red-shifted absorption than the corresponding TTT-extended ones,²² indicating the effective bandgap narrowing for DTP unit.²⁹ The extended absorption can be attributed to more intense ICT effect generated by the replacement of one thiophene ring in TTT with pyrrole ring in DTP.

Energy level diagram of three FREAs is shown in Fig. 2b, with cyclic voltammetry traces plotted in Fig. S31b (ESI†). The highest occupied molecular orbit (HOMO) and lowest unoccupied molecular orbit (LUMO) energy levels are calculated from ionization potentials and electron affinities and calibrated by ferrocene/ferrocenium (Fc/Fc⁺) redox couple, respectively. The HOMO energy levels of **IPT-2F**, **IPTT-2F**, and **IPTTT-2F** show an elevation along with the extension of π -conjugation, while the LUMO energy levels show a down-shifted trend. The relatively subtle variations of LUMO level do not correlate completely with the empirical rule that LUMO lift accompanied as a function of intensifying donor cores. Interestingly, V_{oc} values of devices (presented below) show a gradual promotion from IPT-2F, IPTT-2F to IPTTT-2F. Similar case is also found in asymmetric FREAs of TPTTT-2F and TPTTTT-2F.^{22,43} We consider that these phenomena are the special properties, which are presented when asymmetric core extensions are conducted in the cores containing strong and dominant donor block such as DTP or TTT. Differential scanning calorimeter (DSC) analysis shows that only **IPT-2F** has an obvious crystallization temperature (T_c) of 205.2°C with a melting temperature (T_m) at 211.4°C (Fig. S31c). The result indicates that a shorter π -conjugation length of **IPT-2F** makes molecular relaxation easier. With larger donating cores, the rigid **IPTT-2F** and **IPTTT-2F** can't enjoy molecular relaxation and movement even heated upto their decomposition temperatures. The particular molecular relaxation of **IPT-2F** may be a reason of the higher FF and J_{SC} as discussed below.

To evaluate the photovoltaic properties of the asymmetric NFAs, the OSCs were constructed with a conventional architecture of indium tin oxide (ITO)/PEDOT:PSS/PBDB-T:acceptors/Phen-NaDPO/Ag.⁴⁴ The optimum active layers were obtained by spin-coating the PBDB-T:acceptors (1:1, w/w) blend solution in chlorobenzene (CB) with 0.5% (v/v) 1,8-diiodooctane as solvent additive, followed by a thermal annealing step at 100°C for 10 min. The optimization data of the devices was summarized in Table S2-S4 (ESI†). Impressively, the champion PCE of 14.0% with a V_{oc} of 860 mV, and a J_{SC} of 22.4 mA cm⁻² along with a FF of 72.4% was obtained for the **IPT-2F**-based OSCs. A moderate PCE of 12.3% and

a lower PCE of 11.4% were achieved for the **IPTTT-2F**- and **IPTT-2F**-based OSCs, respectively. To the best of our knowledge, 14% PCE is by far the highest PCE value for binary OSCs with asymmetric FREAs (Table S5, ESI†). In comparison to literature-reported best FREAs bearing asymmetric D cores such as a-BTTC,²⁶ TPTTT-2F,²² and SePTTT-2F,²⁷ our IPT-2F exhibits better PCE when blending with PBDB-T or its analogue polymer donors, which is largely attributed to its significantly higher J_{SC} . This may indicate the advantage of incorporating pyrrole unit inside the fused D core to induce intense ICT effect. When compared with DTP-based FREAs (Table S6, ESI†), one can find IPT-2F outperform its symmetric counterparts with higher high J_{SC} and FF values.

A close look at the photovoltaic parameters for our asymmetric FREAs, one can find that **IPT-2F**-based OSCs exhibited the highest J_{SC} and FF. It's known that the J_{SC} can be boosted by broadening photoresponse range of the FREAs²², which agrees well with the absorption results of **IPT-2F** in Fig. 2. The high J_{SC} value may be also attributed to the crystalline nature of **IPT-2F**. The higher FF values of **IPT-2F**- and **IPTTT-2F**-based OSCs are indicators of better blend morphology formed in these S-shaped FREAs blend systems. The low PCE along with an undesirable FF of 66.2% for **IPTT-2F**-based OSCs was probably a result of heterogeneous blend aggregation induced by disadvantageous C-shape conformation. It is thus evident that photovoltaic parameters of asymmetric FREAs based OSCs possess direct relevance to their conformation tuning.

The corresponding current density-voltage (J - V) characteristics are shown in Fig. 3a, with the key photovoltaic parameters listed in Table 2. Compared with **IPTT-2F**- and **IPTTT-2F**, **IPT-2F** based OSCs yielded a slightly reduced V_{OC} but dramatically increased J_{SC} . As shown in Fig. 3b, the external quantum efficiencies (EQEs) spectra of three FREAs based OSCs exhibited strong photoresponse across the whole spectral range, and the maximum EQE value of 82% is observed for **IPT-2F**-based OSCs at 810 nm. The integrated J_{SC} values of **IPT-2F**-, **IPTT-2F**-, and **IPTTT-2F**-based OSCs are 21.2, 19.0, and 19.2 mA cm^{-2} , respectively, consistent with the J_{SC} obtained J - V measurement (within 5% mismatch).

Table 2 Photovoltaic parameters of the PBDB-T:acceptor based OSCs.

Acceptor	J_{SC} [mA cm^{-2}]	J_{SC}^a [mA cm^{-2}]	V_{OC} [mV]	FF [%]	PCE ^b [%]
IPT-2F	22.4 (21.9 ± 0.4)	21.2	860 (853 ± 6)	72.4 (71.5 ± 1.9)	14.0 (13.7 ± 0.3)
IPTT-2F	19.7 (18.9 ± 0.7)	19.0	874 (862 ± 15)	66.2 (63.4 ± 3.8)	11.4 (11.0 ± 0.3)
IPTTT-2F	20.0 (19.3 ± 0.6)	19.2	894 (885 ± 12)	69.3 (67.4 ± 2.6)	12.3 (12.0 ± 0.3)

^a J_{SC} integrated from EQE curves. ^b Average PCE values calculated from ten devices.

To investigate the influence of the conformation reversal on the charge transport properties of the three asymmetric FREAs based blend films, we obtained the electron/hole mobilities (μ_e/μ_h) with space charge limited current (SCLC) measurement. The μ_e/μ_h of PBDB-T blend films with **IPT-2F**, **IPTT-2F**, and **IPTTT-2F** is $3.26 \times 10^{-4}/3.17 \times 10^{-4}$, $3.31 \times 10^{-4}/3.96 \times 10^{-4}$, and $4.48 \times 10^{-4}/4.68 \times 10^{-4} \text{ cm}^2 \text{ V}^{-1} \text{ s}^{-1}$, corresponding to a μ_e/μ_h value of 1.03, 0.84, and 0.96, respectively (Fig. S32, ESI†). Both μ_e and μ_h are

enhanced with the extension of π -conjugation. However, the J_{SC} do not follow the tendency in OSCs. Even so, the μ_e/μ_h values of blend films based on S-shape **IPT-2F** and **IPTTT-2F** are more balanced than the C-shape **IPTT-2F** blend film. A balanced μ_e/μ_h value serves for the yield of high J_{SC} and FF. Similar phenomenon can be found when comparing C-shape TPTTT-2F⁴³ with S-shape TPTTT-2F,²² where the latter shows lower charge mobilities but more balanced μ_e/μ_h value to yield higher J_{SC} and PCE in OSCs.

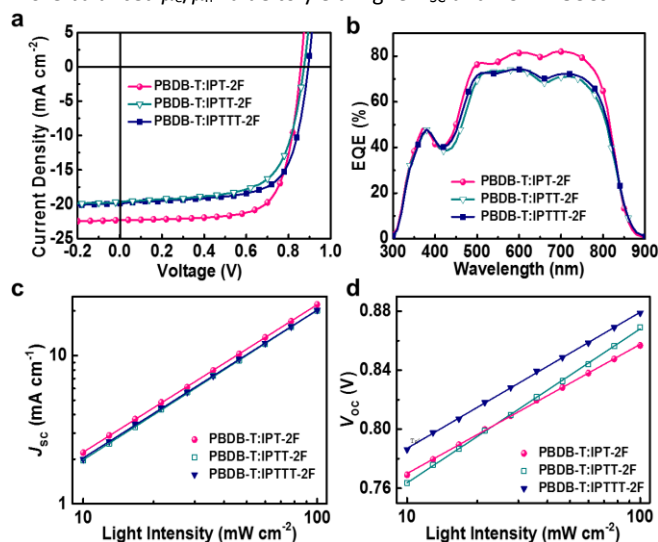


Fig. 3 (a) J - V curves. (b) EQE curves. (c) J_{SC} versus light intensity of the optimized OSCs. (d) V_{OC} versus light intensity of the optimized OSCs.

The effect of bimolecular recombination behaviour on current extraction can be described by $J_{SC} \propto P^{S,45,46}$. A linear relation between J_{SC} and P (light intensity) represents the slope (S) equal to 1, which means an excellent ability of charge extraction. The devices based on **IPT-2F**, **IPTT-2F**, and **IPTTT-2F** all have the S approximate to 0.99, which means bimolecular recombination is not a key defect for the OSCs performance (Fig. 3c). The trap-assisted recombination behaviours obtained from V_{OC} versus light intensity show an obvious pertinence with the conformation reversals. **IPTT-2F**-based OSCs feature a slope of 1.54 kT q^{-1} , whereas we find smaller slopes of 1.34 and 1.42 kT q^{-1} for **IPT-2F**- and **IPTTT-2F**-based OSCs, respectively (Fig. 3d). The smaller slopes for the S-shape NFAs are indicative of less trap-assisted recombination,⁴⁷ which means trap state in the active layer does less damage to the charge carrier, and thus conduces to a higher level of FF and J_{SC} .⁴⁸

GIWAXS was performed to investigate the aggregation behaviours of PBDB-T and the three acceptors in neat and blend films (Fig. S33 in ESI†, Fig. 4). As shown in Fig. S33, neat films of **IPT-2F**, **IPTT-2F**, and **IPTTT-2F** present (010) peaks at 1.8 \AA^{-1} in the out-of-plane (OOP) direction, and the C-shape **IPTT-2F** shows a slightly enhanced (010) π - π stacking peak. However, in the in-plane (IP) direction, S-shape **IPT-2F** and **IPTTT-2F** exhibit quite obvious (100) lamellar stacking at $q_r = 0.33$ and 0.31 \AA^{-1} , corresponding to similar separation distance of 1.9 and 2.0 nm via $d = 2\pi/q$, respectively. Meanwhile, the (100) lamellar stacking for C-shape **IPTT-2F** obtains a lower q_r of 0.25 \AA^{-1} with a large separation distance of 2.5 nm, which represents an incompact

lamellar stacking for face-on packing structure. All three blend films have approximate (010) peak at 1.75 \AA^{-1} in the OOP direction and (100) peak at 0.29 \AA^{-1} in the IP direction. ~~However, compared to IPT-2F and IPTTT-2F based blend, the (010) peak and (100) peak of C-shape IPTT-2F blend film show a relatively flat curve in OOP direction, which means a less ordered packing structure. The obviously enhanced face-on π - π stacking of the blend system relative to corresponding pure film, especially for the S-shape IPT-2F- and IPTTT-2F-based blend, can be attributed to the effective synergy coming from both polymer donor and S-shape NFAs. The intervention of PBDB-T assists the face-on π - π stacking of the blend system, especially for the S-shape IPT-2F and IPTTT-2F based blend.~~ In general, the more well-organized and compact packing structure can be responsible for the less trap-assisted recombination and higher FF values in IPT-2F- and IPTTT-2F-based devices. To understand the mesoscale morphology of these blend films, resonant soft X-ray scattering (R-SoXS) with 284.8 eV photon energy is used to compare their compositional domain characteristics (Fig. 4c). A quite strong and broad scattering profile is presented in PBDB-T:IPTT-2F blend film. And a scattering hump at $\sim 0.0055 \text{ \AA}^{-1}$ is seen, which means an average length-scale phase separation at 114 nm. Furthermore, the broad scattering profile represents a wide distribution of length-scale phase separation, which indicates the heterogeneity of domain size. Yet the scattering profiles of PBDB-T:IPT-2F and PBDB-T:IPTTT-2F blends all show weak but narrow peak with a scattering hump at $\sim 0.007 \text{ \AA}^{-1}$ corresponding to a relatively small length-scale phase separation of 90 nm. These results indicate C-shaped IPTT-2F-based blend has enhanced domain size and domain purity, but heterogeneous and large domain separation, thus leading to the detrimental charge recombination. On the contrary, S-shaped IPT-2F- and IPTT-2F-based blends obtain the best morphology with proper domain size and uniformity, thus making the devices achieve higher FF and J_{sc} . In addition, compared to IPTTT-2F-based blend, the PBDB-T:IPT-2F blend has a more dominant face-on orientation and better domain properties, which can explain the better performance of IPT-2F-based devices.

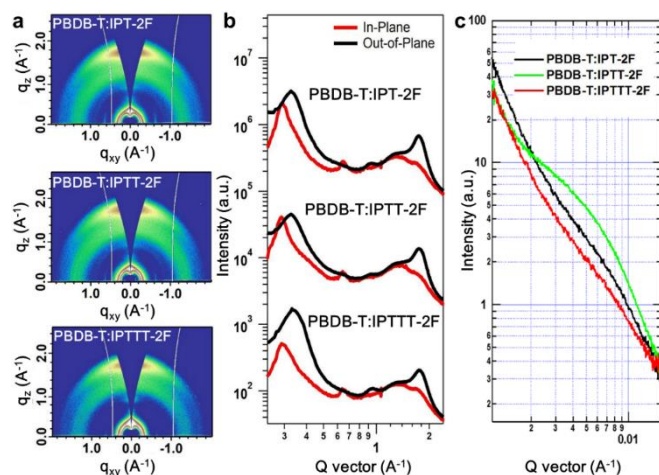


Fig. 4 (a) GIWAXS patterns of PBDB-T:IPT-2F, PBDB-T:IPTT-2F, and PBDB-T:IPTTT-2F blend films. (b) Corresponding line cuts of the GIWAXS images. (c) R-SoXS profiles in log scale for the blend films.

To intuitively understand the influence of molecular conformation on device performance, morphology characteristics of the blend films were mapped by atomic force microscope (AFM) in tapping mode. As shown in Fig. 5, the blend films based on IPT-2F, IPTT-2F, and IPTTT-2F all have a small root-mean-square surface roughness (R_q) value from the respective height image. PBDB-T:IPT-2F blend film assembled a local order textures of long fibril type, thus benefiting to the exciton dissociation and charge transport in active layer.^{49,50} The blend film of PBDB-T:IPTTT-2F formed a non-fibrous but orderly and homogeneous microphase separation in a small length scale, which is a suboptimal morphology for device performance. In sharp contrast to the morphologies above, the blend film based on C-shape IPTT-2F presents an irregular macrophase separation and an unordered phase arrangement that make the blend lack enough channels for charge transport and generate large recombination losses.⁵¹ The TEM images show IPT-2F- and IPTTT-2F-based blends possess relatively more fine structure of phase separation, while IPTT-2F-based blend shows heterogeneous morphology (Fig. S34 in ESI[†]), which are consistent with the AFM and R-SoXS tests. The morphology results readily explain the significantly higher J_{sc} and FF obtained for IPT-2F- and IPTTT-2F-based OSCs, i.e., appropriate NFAs conformation tunes intermolecular interactions and aggregations in bulk heterojunction blends to promote nanofibril morphology and thus better charge transport/separation. All experimental and simulation data agree well with the finding that molecular conformation tuning of asymmetric FREAs can induce better molecular packing, blend morphology and thus photovoltaic performance.

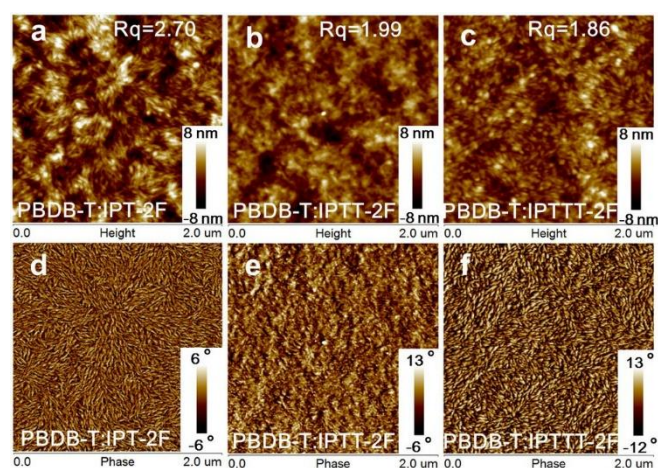


Fig. 5 (a-c) AFM height images of the blend films. (d-f) AFM phase images of the blend films.

3. Conclusion

In summary, for the first time we have introduced the concept of tuning conformation of asymmetric nonfullerene

acceptors by developing dithieno[3,2-*b*:2',3'-*d*]pyrrol fused 7-, 8- and 9-ring structured electronic acceptors. The intermolecular weak S...O interactions induce the molecular conformation reversal when gradually extending fused-ring core with thiophene unit. The S-shaped NFAs with accepting terminals aligning in parallel along the core axis exhibit improved molecular packing in solid state. Evident molecular conformation affecting photovoltaic performance has been demonstrated in OSCs by blending DTP-based asymmetric NFAs with PBDB-T as polymer donor. Importantly, PBDB-T blends with either **IPT-2F** or **IPTTT-2F** featuring S-shape conformation exhibit perfect nanofibril morphology with homogeneous and regular phase separation, while heterogeneous blend phase structure was detected for C-shaped IPTT-2F. Impressively, **IPT-2F**-based binary OSCs contribute a maximum PCE of 14% with high J_{SC} of 22.4 mA cm⁻² and FF of 72.4%. These values, to the best of our acknowledgment, are among the highest ones for asymmetric NFA based devices. The enhanced performance is attributed to more balanced charge transport and reduced trap-assisted recombination in devices. Our results indicate the conformation tuning to reinforce intermolecular interactions may open a new avenue for FREAs design in the pursuit of high-performance OSCs.

4. Experimental

Synthesis of IPT-2F. Compound IPT-CHO (130.0 mg, 111.0 μ mol), 2-(5/6-fluoro-3-oxo-2,3-dihydro-1H-inden-1-ylidene) malononitrile (117.8 mg, 555.2 μ mol) and β -alanine (2.0 mg, 22.2 μ mol) were dissolved in a mixed solvent of 1,2-dichloroethane (8 mL) and EtOH (3 mL). The mixture was placed at 60°C for several hours and the reaction process was monitored by TLC. The solvent in the mixture was evaporated under vacuum. The residue was purified by silica gel column chromatography (petroleum ether/dichloromethane=3:2 v/v) to obtain a dark-blue solid (146 mg, 84%). ¹H NMR (500 MHz, CDCl₃, δ): 8.86 (m, 2H), 8.70 - 8.60 (m, 0.5H), 8.37 - 8.30 (m, 1.5H), 7.90 - 7.82 (m, 1.5H), 7.69 - 7.67 (m, 2H), 7.58 - 7.47 (m, 2.5H), 7.39 (m, 1H), 7.33 - 7.30 (m, 5H), 7.16 - 7.11 (m, 12H), 3.78 (t, J = 8.1 Hz, 2H), 2.59 (m, 8H), 1.60 (m, 8H), 1.38 - 1.26 (m, 28H), 1.24 - 1.15 (m, 4H), 1.12 - 0.99 (m, 4H), 0.88 (m, 15H). ¹³C NMR (125 MHz, CDCl₃, δ): 187.16, 187.05, 167.90, 165.85, 165.65, 160.70, 159.49, 159.47, 159.45, 159.17, 159.16, 159.14, 158.53, 157.82, 157.79, 156.54, 150.43, 150.40, 147.27, 147.23, 146.71, 142.87, 142.54, 142.51, 142.47, 142.39, 140.91, 140.87, 140.66, 140.55, 140.03, 140.00, 138.78, 138.73, 138.58, 137.21, 136.62, 135.99, 135.55, 135.51, 134.72, 133.28, 133.16, 133.15, 128.94, 128.92, 128.66, 127.92, 126.09, 126.01, 125.94, 125.61, 125.54, 121.97, 121.77, 121.74, 121.67, 121.35, 121.15, 120.34, 120.29, 118.92, 118.91, 117.65, 115.46, 115.33, 115.04, 114.57, 114.48, 113.07, 112.86, 112.83, 112.62, 69.73, 67.62, 67.61, 63.12, 62.78, 62.77, 48.73, 35.76, 35.73, 32.07, 31.90, 31.88, 31.51, 31.46, 30.64, 29.54, 29.44, 29.35, 29.30, 26.98, 22.86, 22.79, 14.31, 14.29. ¹⁹F NMR (470 MHz, CDCl₃, δ): -99.01, -99.02, -99.04, -99.05, -100.08, -100.10, -100.11, -100.13, -100.35, -101.31. MALDI-TOF MS (m/z): [M+H]⁺ calcd. for C₁₀₂H₉₇F₂N₅O₂S₃, 1557.6772; found, 1557.6766.

Synthesis of IPTT-2F: By utilizing the similar synthetic method as used for **IPT-2F**, compound IPTT-CHO (130.0 mg, 106.0 μ mol)

and 2-(5/6-fluoro-3-oxo-2,3-dihydro-1H-inden-1-ylidene) malononitrile (112.4 mg, 529.8 μ mol) and β -alanine (1.9 mg, 21.2 μ mol) were used for the synthesis of **IPTT-2F**. The target compound was obtained as a dark-blue solid (140 mg, 81%). ¹H NMR (500 MHz, CDCl₃, δ): 8.84 (m, 2H), 8.69 - 8.60 (m, 0.5H), 8.35 - 8.29 (m, 1.5H), 8.20 - 8.18 (m, 1H), 7.91 - 7.81 (m, 1.5H), 7.62 - 7.46 (m, 3.5H), 7.41 - 7.27 (m, 6H), 7.21 (d, J = 8.5 Hz, 4H), 7.16 - 7.14 (m, 8H), 3.80 - 3.74 (m, 2H), 2.58 (m, 8H), 1.63 - 1.57 (m, 8H), 1.37 - 1.26 (m, 28H), 1.23 - 1.15 (m, 4H), 1.13 - 0.99 (m, 4H), 0.90 - 0.85 (m, 15H). ¹³C NMR (125 MHz, CDCl₃, δ): 187.06, 186.95, 186.85, 167.88, 167.68, 167.29, 165.83, 165.64, 165.41, 165.23, 159.97, 159.48, 159.13, 159.11, 158.27, 155.73, 153.94, 153.89, 150.79, 147.89, 147.73, 147.45, 147.41, 146.65, 143.71, 142.85, 142.66, 142.54, 142.46, 140.12, 139.54, 139.52, 139.15, 138.66, 138.55, 138.46, 137.46, 137.42, 137.37, 136.56, 136.45, 136.07, 135.99, 135.97, 134.97, 134.78, 133.25, 133.24, 133.15, 133.14, 129.04, 129.04, 128.91, 128.71, 128.08, 126.07, 125.99, 125.57, 125.49, 124.61, 122.47, 122.38, 122.02, 121.83, 121.69, 121.51, 121.28, 121.09, 120.22, 120.19, 120.13, 119.98, 119.94, 119.84, 117.74, 117.42, 115.53, 115.40, 115.11, 114.52, 114.44, 113.02, 112.81, 112.59, 70.04, 67.38, 63.35, 62.89, 48.71, 35.80, 35.73, 32.08, 31.90, 31.88, 31.45, 31.43, 29.55, 29.45, 29.38, 29.37, 27.00, 22.86, 22.79, 14.31, 14.28. ¹⁹F NMR (470 MHz, CDCl₃, δ): -98.88, -98.90, -98.91, -100.18, -100.24, -100.25, -101.45. MALDI-TOF MS (m/z): [M+H]⁺ calcd. for C₁₀₄H₉₇F₂N₅O₂S₄, 1613.6493; found, 1613.6489.

Synthesis of IPTTT-2F: By utilizing the similar synthetic method as used for **IPT-2F**, compound IPTTT-CHO (130.0 mg, 101.3 μ mol) and 2-(5/6-fluoro-3-oxo-2,3-dihydro-1H-inden-1-ylidene)malononitrile (107.5 mg, 506.7 μ mol) and β -alanine (1.8 mg, 20.3 μ mol) were used for the synthesis of **IPTTT-2F**. The target compound was obtained as a dark-blue solid (143 mg, 84%). ¹H NMR (500 MHz, CDCl₃, δ): 8.90 - 8.79 (m, 2H), 8.56 - 8.62 (m, 0.5H), 8.32 - 8.25 (m, 1.5H), 7.90 - 7.77 (m, 3H), 7.57 (s, 2H), 7.52 - 7.44 (m, 1H), 7.36 (d, J = 8.2 Hz, 4H), 7.32 - 7.27 (m, 1.5H), 7.24 (m, 0.5H), 7.19 - 7.15 (m, 8H), 7.13 (d, J = 8.2 Hz, 4H), 3.77 (t, J = 8.2 Hz, 2H), 2.59 (m, 8H), 1.66 - 1.56 (m, 8H), 1.37 - 1.26 (m, 28H), 1.24 - 1.17 (m, 4H), 1.13 - 1.03 (m, 4H), 0.88 (m, 15H). ¹³C NMR (125 MHz, CDCl₃, δ): 187.15, 187.06, 186.94, 167.90, 167.63, 165.85, 165.59, 159.45, 158.82, 158.30, 154.84, 151.15, 149.03, 149.00, 148.32, 147.63, 147.60, 146.61, 143.47, 143.43, 142.98, 142.95, 142.82, 142.69, 142.54, 142.46, 139.79, 139.19, 138.44, 138.28, 138.12, 138.08, 137.65, 137.51, 136.94, 136.69, 136.33, 133.23, 133.19, 133.15, 133.11, 133.09, 133.09, 128.97, 128.92, 128.75, 128.10, 126.07, 125.99, 125.48, 125.40, 122.16, 122.09, 121.94, 121.75, 121.16, 120.98, 119.97, 119.74, 119.69, 117.31, 117.17, 115.57, 115.45, 115.15, 114.53, 114.37, 112.75, 112.54, 70.17, 67.20, 63.37, 62.93, 48.71, 35.79, 35.75, 32.09, 31.89, 31.46, 31.43, 30.62, 29.56, 29.46, 29.38, 29.34, 27.01, 22.87, 22.80, 22.78, 14.32, 14.28. ¹⁹F NMR (470 MHz, CDCl₃, δ): -98.65, -98.66, -98.67, -100.12, -100.30, -100.32, -100.33, -101.55. MALDI-TOF MS (m/z): [M+H]⁺ calcd. for C₁₀₆H₉₇F₂N₅O₂S₅, 1669.6214; found, 1669.6209.

Conflicts of interest

There are no conflicts to declare.

Acknowledgements

L. Y. and X. S. contributed equally to this work. The authors gratefully acknowledge the financial support from the National Natural Science Foundation of China (Grant No. 51573077, 21875111 and 51861145401), Jiangsu Province Natural Science Foundation (BK20180496), the 333 Project to Cultivate High Level Talents in Jiangsu Province, and the Priority Academic Program Development of Jiangsu Higher Education Institutions.

Notes and references

- G. Yu, J. Gao, J. C. Hummelen, F. Wudl and A. J. Heeger, *Science*, 1995, **270**, 1789-1791.
- K. A. Mazzio and C. K. Luscombe, *Chem. Soc. Rev.*, 2015, **44**, 78-90.
- G. Zhang, J. Zhao, P. C. Y. Chow, K. Jiang, J. Zhang, Z. Zhu, J. Zhang, F. Huang and H. Yan, *Chem. Rev.*, 2018, **118**, 3447-3507.
- A. Wadsworth, M. Moser, A. Marks, M. S. Little, N. Gasparini, C. J. Brabec, D. Baran and I. McCulloch, *Chem. Soc. Rev.*, 2019, **48**, 1596-1625.
- J. Yuan, Y. Zhang, L. Zhou, G. Zhang, H.-L. Yip, T.-K. Lau, X. Lu, C. Zhu, H. Peng, P. A. Johnson, M. Leclerc, Y. Cao, J. Ullanski, Y. Li and Y. Zou, *Joule*, 2019, **3**, 1140-1151.
- B. Fan, D. Zhang, M. Li, W. Zhong, Z. Zeng, L. Ying, F. Huang and Y. Cao, *Sci. China Chem.*, 2019, **62**, 746-752.
- R. Yu, H. Yao, Y. Cui, L. Hong, C. He and J. Hou, *Adv. Mater.*, 2019, 1902302.
- Y. Cui, H. Yao, L. Hong, T. Zhang, Y. Xu, K. Xian, B. Gao, J. Qin, J. Zhang, Z. Wei and J. Hou, *Adv. Mater.*, 2019, **31**, 1808356.
- Q. An, X. Ma, J. Guo and F. Zhang, *Sci. Bull.*, 2019, **64**, 504-506.
- Y. Lin, Q. He, F. Zhao, L. Huo, J. Mai, X. Lu, C. J. Su, T. Li, J. Wang, J. Zhu, Y. Sun, C. Wang and X. Zhan, *J. Am. Chem. Soc.*, 2016, **138**, 2973-2976.
- C. Yan, S. Barlow, Z. Wang, H. Yan, A. K. Y. Jen, S. R. Marder and X. Zhan, *Nat. Rev. Mater.*, 2018, **3**, 18003.
- Y. Lin, J. Wang, Z.-G. Zhang, H. Bai, Y. Li, D. Zhu and X. Zhan, *Adv. Mater.*, 2015, **27**, 1170-1174.
- S. Dai, F. Zhao, Q. Zhang, T.-K. Lau, T. Li, K. Liu, Q. Ling, C. Wang, X. Lu, W. You and X. Zhan, *J. Am. Chem. Soc.*, 2017, **139**, 1336-1343.
- W. Zhao, S. Li, H. Yao, S. Zhang, Y. Zhang, B. Yang and J. Hou, *J. Am. Chem. Soc.*, 2017, **139**, 7148-7151.
- Z. Zhang, J. Yu, X. Yin, Z. Hu, Y. Jiang, J. Sun, J. Zhou, F. Zhang, T. P. Russell, F. Liu and W. Tang, *Adv. Funct. Mater.*, 2018, **28**, 1705095.
- S. Dai, Y. Xiao, P. Xue, J. James Rech, K. Liu, Z. Li, X. Lu, W. You and X. Zhan, *Chem. Mater.*, 2018, **30**, 5390-5396.
- Z. Xiao, S. Yang, Z. Yang, J. Yang, H. L. Yip, F. Zhang, F. He, T. Wang, J. Wang, Y. Yuan, H. Yang, M. Wang and L. Ding, *Adv. Mater.*, 2018, 1804790.
- X. Shi, X. Liao, K. Gao, L. Zuo, J. Chen, J. Zhao, F. Liu, Y. Chen and A. K. Y. Jen, *Adv. Funct. Mater.*, 2018, **28**, 1802324.
- H. Wang, J. Cao, J. Yu, Z. Zhang, R. Geng, L. Yang and W. Tang, *J. Mater. Chem. A*, 2019, **7**, 4313-4333.
- H. Yao, Y. Chen, Y. Qin, R. Yu, Y. Cui, B. Yang, S. Li, K. Zhang and J. Hou, *Adv. Mater.*, 2016, **28**, 8283-8287.
- W. Gao, T. Liu, C. Zhong, G. Zhang, Y. Zhang, R. Ming, L. Zhang, J. Xin, K. Wu, Y. Guo, W. Ma, H. Yan, Y. Liu and C. Yang, *ACS Energy Lett.*, 2018, **3**, 1760-1768.
- J. Song, C. Li, L. Ye, C. Koh, Y. Cai, D. Wei, H. Y. Woo and Y. Sun, *J. Mater. Chem. A*, 2018, **6**, 18847-18852.
- W. Gao, Q. An, C. Zhong, Z. Luo, R. Ming, M. Zhang, Y. Zou, F. Liu, F. Zhang and C. Yang, *Chem. Sci.*, 2018, **9**, 8142-8149.
- W. Gao, M. Zhang, T. Liu, R. Ming, Q. An, K. Wu, D. Xie, Z. Luo, C. Zhong, F. Liu, F. Zhang, H. Yan and C. Yang, *Adv. Mater.*, 2018, **30**, 1800052.
- C. Li, H. Fu, T. Xia and Y. Sun, *Adv. Energy Mater.*, 2019, **9**, 190999.
- W. Gao, T. Liu, J. Li, Y. Xiao, G. Zhang, Y. Chen, C. Zhong, X. Lu, H. Yan and C. Yang, *J. Mater. Chem. A*, 2019, **7**, 11053-11061.
- C. Li, T. Xia, J. Song, H. Fu, H. S. Ryu, K. Weng, L. Ye, H. Y. Woo and Y. Sun, *J. Mater. Chem. A*, 2019, **7**, 1435-1441.
- C. Huang, X. Liao, K. Gao, L. Zuo, F. Lin, X. Shi, C.-Z. Li, H. Liu, X. Li, F. Liu, Y. Chen, H. Chen and A. K. Y. Jen, *Chem. Mater.*, 2018, **30**, 5429-5434.
- Y. Geng, A. Tang, K. Tajima, Q. Zeng and E. Zhou, *J. Mater. Chem. A*, 2019, **7**, 64-96.
- J. Sun, X. Ma, Z. Zhang, J. Yu, J. Zhou, X. Yin, L. Yang, R. Geng, R. Zhu, F. Zhang and W. Tang, *Adv. Mater.*, 2018, **30**, 1707150.
- R. Geng, X. Song, H. Feng, J. Yu, M. Zhang, N. Gasparini, Z. Zhang, F. Liu, D. Baran and W. Tang, *ACS Energy Lett.*, 2019, **4**, 763-770.
- H. Feng, X. Song, M. Zhang, J. Yu, Z. Zhang, R. Geng, L. Yang, F. Liu, D. Baran and W. Tang, *Mater. Chem. Front.*, 2019, **3**, 702-708.
- X. Ma, W. Gao, J. Yu, Q. An, M. Zhang, Z. Hu, J. Wang, W. Tang, C. Yang and F. Zhang, *Energy Environ. Sci.*, 2018, **11**, 2134-2141.
- W. Li, M. Chen, Z. Zhang, J. Cai, H. Zhang, R. S. Gurney, D. Liu, J. Yu, W. Tang and T. Wang, *Adv. Funct. Mater.*, 2019, **29**, 1807662.
- M. Chen, Z. Zhang, W. Li, J. Cai, J. Yu, E. Spooner, R. Kilbride, D. Li, B. Du, R. Gurney, D. Liu, W. Tang, D. Lidzey and T. Wang, *Sci. China Chem.*, 2019, DOI: 10.1007/s11426-019-9484-8.
- H. Huang, Z. Chen, R. P. Ortiz, C. Newman, H. Usta, S. Lou, J. Youn, Y.-Y. Noh, K.-J. Baeg, L. X. Chen, R. P. Chang, A. Facchetti and T. J. Marks, *J. Am. Chem. Soc.*, 2012, **134**, 10966-10973.
- X. Shi, L. Zuo, S. B. Jo, K. Gao, F. Lin, F. Liu and A. K. Y. Jen, *Chem. Mater.*, 2017, **29**, 8369-8376.
- Y. Liu, C. e. Zhang, D. Hao, Z. Zhang, L. Wu, M. Li, S. Feng, X. Xu, F. Liu, X. Chen and Z. Bo, *Chem. Mater.*, 2018, **30**, 4307-4312.
- T. Lu and F. Chen, *J. Mol. Graph. Model.*, 2012, **38**, 314-323.
- T. Lu and F. Chen, *J. Comput. Chem.*, 2012, **33**, 580-592.
- J. E. Coughlin, A. Zhugayevych, R. C. Bakus, T. S. van der Poll, G. C. Welch, S. J. Teat, G. C. Bazan and S. Tretiak, *J. Phys. Chem. C*, 2014, **118**, 15610-15623.
- S. Yu, Y. Chen, L. Yang, P. Ye, J. Wu, J. Yu, S. Zhang, Y. Gao and H. Huang, *J. Mater. Chem. A*, 2017, **5**, 21674-21678.
- C. Li, J. Song, L. Ye, C. Koh, K. Weng, H. Fu, Y. Cai, Y. Xie, D. Wei, H. Y. Woo and Y. Sun, *Solar RRL*, 2019, **3**, 1800246.
- X. Song, N. Gasparini, M. M. Nahid, S. H. K. Paleti, J.-L. Wang, H. Ade and D. Baran, *Joule*, 2019, **3**, 846-857.
- P. Schilinsky, C. Waldauf and C. J. Brabec, *Appl. Phys. Lett.*, 2002, **81**, 3885-3887.
- L. J. A. Koster, V. D. Mihailetschi, R. Ramaker and P. W. M. Blom, *Appl. Phys. Lett.*, 2005, **86**, 123509.
- N. Gasparini, M. Salvador, S. Strohm, T. Heumueller, I. Levchuk, A. Wadsworth, J. H. Bannock, J. C. de Mello, H.-J.

- Egelhaaf, D. Baran, I. McCulloch and C. J. Brabec, *Adv. Energy Mater.*, 2017, **7**, 1700770.
- 48 R. S. Gurney, D. G. Lidzey and T. Wang, *Rep. Prog. Phys.*, 2019, **82**, 036601.
- 49 G. Han, Y. Yi and Z. Shuai, *Adv. Energy Mater.*, 2018, **8**, 1702743
- 50 L. Ye, B. A. Collins, X. Jiao, J. Zhao, H. Yan and H. Ade, *Adv. Energy Mater.*, 2018, **8**, 1703058.
- 51 F. Zhao, C. Wang and X. Zhan, *Adv. Energy Mater.*, 2018, **8**, 1703147.